



# Annealing-Mediated Microduplex Structure and Texture Evolution in Severely Cold-Rolled Nanolamellar Pearlite: A Perspective on the Effect of Starting Inter-lamellar Spacing

R. HAMSHINI, B. TRIPATHY, S. PAUL, S. NARAYANSWAMY, R. SAHA, and P.P. BHATTACHARJEE

The effect of inter-lamellar (IL) spacing on the microstructure and texture of severely cold-rolled and annealed pearlite was studied. For this purpose, the behavior of fine IL spacing starting material (FILSM) (~ 190 nm) was compared with a coarser IL spacing starting material (CILSM) (~ 275 nm). The materials were severely cold-rolled to 95 pct reduction in thickness and annealed at 973 K (700 °C) for different time intervals. Despite similarities in microstructural evolution featured by progressive alignment of the pearlitic colonies along the rolling direction (RD), bending and kink morphologies, fragmentation of cementite, and deformation-induced nanoscale structure, the FILSM showed a smaller nanoscale IL spacing (~ 45 nm) than CILSM (~ 60 nm) after severe cold-rolling. Both FILSM and CILSM showed similar deformation texture featured by the presence of typical ND ( $// <111>$ ) and RD ( $// <110>$ ) fibers. Annealing of the severely cold-rolled materials resulted in an ultrafine microduplex structure. However, annealed FILSM consistently showed lower ferrite and spheroidized cementite sizes than those in the annealed CILSM. Irrespective of the starting IL spacing, continuous recrystallization was found to be the softening mechanism, which was amply corroborated by the texture evolution during annealing. Therefore, although the starting IL spacing considerably affected the microstructure, the texture evolution remained largely unaffected. The tensile behavior of the microduplex structured FILSM was further analyzed considering Hall–Petch (H–P) and Orowan–Ashby (O–A) strengthening mechanisms.

<https://doi.org/10.1007/s11661-023-06974-5>

© The Minerals, Metals & Materials Society and ASM International 2023

## I. INTRODUCTION

DEVELOPING ultra-high strength materials by grain size reduction is an important area in materials research. The emergence of severe plastic deformation (SPD) processing<sup>[1]</sup> enabled attaining bulk ultrafine-grain (UFG with average grain size  $\bar{d} > 100$  nm) and nanostructure (NS with  $\bar{d} \leq 100$  nm) in a wide variety of materials. Consequently, understanding of the

processing–microstructure–properties relationship in severely deformed bulk UFG and NS alloys<sup>[2–4]</sup> has attracted unprecedented attention.<sup>[5,6]</sup>

In the context of SPD processing, the pearlitic lamellar morphology of ferrite and cementite has been a topic of much interest from academic and industrial perspectives.<sup>[7]</sup> Pearlitic steels subjected to SPD processing by severe wire-drawing and high-pressure torsion (HPT) have been extensively investigated to understand massive nanostructure formation and outstanding strength enhancement.<sup>[8–23]</sup> Interestingly, studies on pearlite processed by conventional rolling deformation are limited. Tagashira *et al.*<sup>[24]</sup> have studied microstructural development in pearlitic steels with carbon contents of 0.76 pctC, 0.6 pctC, and 0.1 pctC subjected to cold-rolling between 70 and 95 pct thickness reduction. The cold-rolled microstructure showed the development of microstructural inhomogeneities characterized by severe bending, thicker lamellae containing shear bands, and finer lamellae. Further annealing of the 1 pctC pearlite resulted in the formation of an ultrafine-grained (Ferrite + cementite) microduplex structure (with grain

R. HAMSHINI, B. TRIPATHY, S. PAUL, and P. P. BHATTACHARJEE are with the Department of Materials Science and Metallurgical Engineering, IIT Hyderabad, Hyderabad, Telangana 502284, India. Contact e-mail: pinakib@msme.iith.ac.in S. NARAYANSWAMY is with the International Advanced Research Centre for Powder Metallurgy and New Materials (ARCI), Hyderabad, Telangana 500005, India. R. SAHA is with the R&D Division, TATA Steel, Jamshedpur, Jharkhand 831001, India

Manuscript submitted July 21, 2022; accepted January 14, 2023.

Article published online February 6, 2023

size less than  $0.5\ \mu\text{m}$ ) in the Fe-1.4Cr-1.0C alloy.<sup>[25]</sup> Narayanaswamy *et al.*<sup>[26]</sup> have studied the deformation and recrystallization behavior of 0.72 pctC pearlitic steel. They have reported a switchover from a discontinuous to a continuous recrystallization behavior in pearlite with increasing cold-rolling strain. The correlation between microduplex structures and strength–ductility relationship in medium carbon steels ranging from 0.36 pct<sup>[27,28]</sup> to 0.48 pctC<sup>[29]</sup> after heavy warm deformation and annealing has been studied. These studies have concluded the formation of homogeneous ultrafine microstructure featured by the fine distribution of cementite within the ultrafine ferrite matrix and remarkable enhancement in mechanical properties. The ultrafine microduplex structure and superior strength–ductility synergy have also been demonstrated in high-carbon steel (0.66 pctC) after heavy warm-rolling and annealing.<sup>[30]</sup> Narayanaswamy *et al.*<sup>[31]</sup> have studied texture evolution accompanying ultrafine microduplex structure evolution in a heavily warm-rolled and annealed pearlitic steel (0.72 pctC) and reported the formation of characteristic texture inhomogeneities featured by the presence of Goss component ( $\{110\} \langle 001 \rangle$ ) at the surface (due to surface shear) and diffuse texture at the interior.

The effect of key microstructural parameters needs to be clarified to understand the complete paradigm of microstructure, texture, and properties. An important parameter is the starting IL spacing. The starting grain size considerably affects the deformation and annealing behavior. As a natural extension, it may be expected that the IL spacing should also affect the microstructure, texture, and mechanical response. Nevertheless, systematic studies focusing on these aspects are quite limited. The present study, therefore, attempts to bridge this knowledge gap. For this purpose, we compare the behavior of completely pearlitic steel with fine inter-lamellar spacing with that of the same steel but having coarse inter-lamellar spacing investigated by Narayanaswamy *et al.*<sup>[26]</sup>. To adequately highlight the effect of starting IL spacing while avoiding repetition of discussion, we only focus on the key results from the previous study<sup>[26]</sup> judiciously.

## II. EXPERIMENTAL

### A. Processing

The chemistry of the as-received steel used for the research is presented in Table I. The steel was austenized at 1223 K (950 °C) for 600 s (10 min (min)) under an inert argon atmosphere and then salt-bath treated at 673 K (400 °C) for  $2.4 \times 10^3$  s (40 min) for pearlitic transformation followed by water quenching. These heat-treated specimens (thickness,  $t \sim 9.6$  mm to 10 mm) were designated as fine inter-lamellar spacing starting materials (FILSM) and subjected to further thermo-mechanical processing. To clarify the inter-lamellar spacing effect, comparisons were made with the same steel (investigated previously by Narayanaswamy *et al.*<sup>[26]</sup>), which was prepared in the same way

**Table I. Chemical Composition (Wt Pct) of the Pearlitic Steel Investigated in this Work**

C	Mn	Si	S	P	N	Fe
0.72	0.75	0.157	0.010	0.020	0.0037	bal

except for being heat-treated at a higher temperature of 923 K (650 °C) for 600 s (10 min). These are referred to as coarse inter-lamellar spacing starting material (CILSM).

Specimens of the FILSM ( $t \sim 9.6$ – $10$  mm) were 95 pct cold-rolled (true equivalent strain ( $\epsilon_{\text{eq}}$ )  $\sim 3.4$ ) to a final thickness of  $\sim 0.43$ – $0.50$  mm using a multi-pass rolling not exceeding 10 pct deformation per pass. A two-high rolling equipment dedicated to laboratory practices (Fenn Division, USA) was used for this purpose.

Microstructure evolution was studied at the intermediate deformation levels of 30 pct, 50 pct, 80 pct, and finally, after 95 pct thickness reductions. The 95 pct cold-rolled sheets were further heat-treated at 973 K (700 °C) for 60 s (1 min) to  $4.32 \times 10^4$  s (720 min) in a molten salt-bath and quenched.

### B. Characterization

The macrotexture of the cold-rolled specimens was studied by X-ray diffraction (Make: Panalytical, Netherlands; Model: Xpert Pro Diffractometer) using Cu  $K_{\alpha}$  radiation. The requisite number of incomplete pole figures (PFs) (110), (200), (211), and (222) were measured and used as input in the MTM-FHM software for determining the orientation distribution function (ODFs) using harmonic series expansion method with a series rank of 22.

The microstructure and microtexture were evaluated by a field emission gun (FEG) scanning electron microscope (FEG-SEM) (Make: JEOL, Japan; Model: JSM 7800F) integrated with an electron backscatter diffraction (EBSD) (EDAX Inc., USA) system. The post-processing analysis of the EBSD dataset was carried out by TSL-OIM™ software (EDAX Inc., USA). Multiple EBSD scans were taken from each specimen to ensure at least 1000 grains were covered in the EBSD analysis, and the scans were merged for analysis purposes. The textures of the different specimens were presented using relevant ODF sections calculated from the EBSD data using the harmonic series expansion method with a series rank of 22. Mechanical polishing (by colloidal silica) succeeded by electro-polishing (temperature:  $-15$  °C; electrolyte: perchloric acid + methanol solution) was employed for EBSD specimen preparation.

## III. RESULTS

### A. Effect of Cold-Rolling

FILSM (Figure 1(a)) depicts a near-complete pearlitic microstructure with an insignificant amount of primary ferrite (white arrow). The inverse pole figure (IPF) map

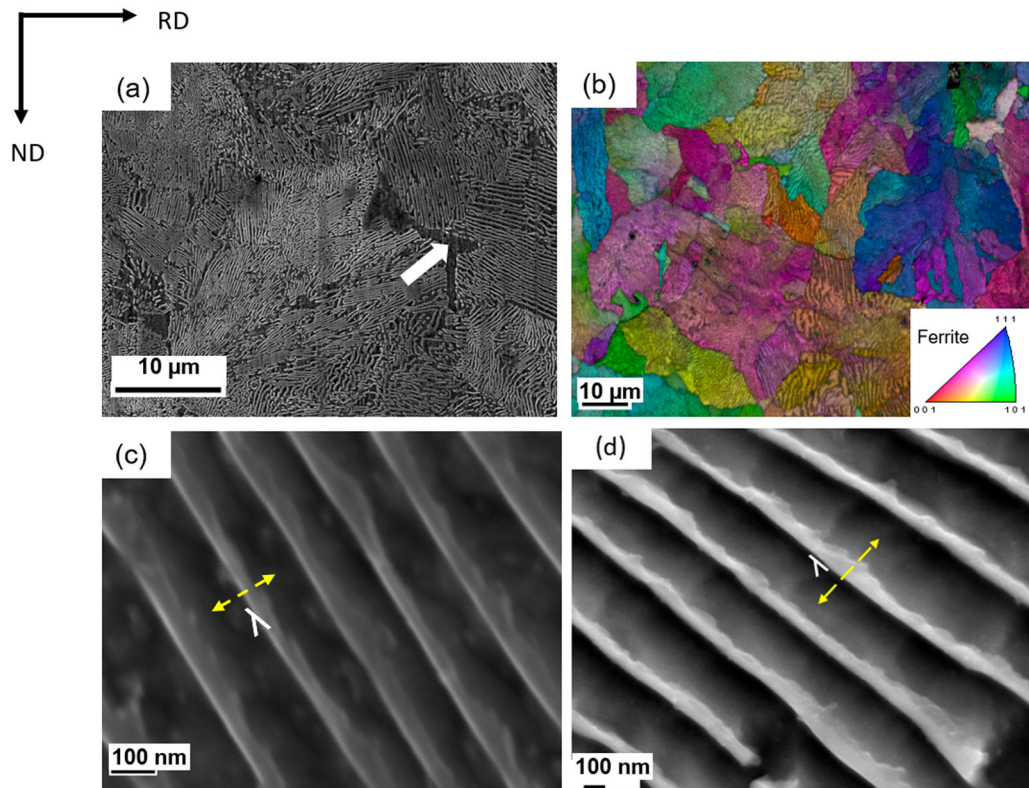


Fig. 1—(a) SEM micrograph, (b) ND-IPF map, and (c) enlarged SEM image showing the IL spacing in FILSM. (d) An enlarged SEM micrograph showing the IL spacing of the CILSM.

(Figure 1(b)) reveals pearlitic colonies with different orientations within the prior austenite grains. A magnified image of the lamellar pearlite arrangement in the SM is represented in Figure 1(c). The mean inter-lamellar spacing ( $\lambda$ ), which is defined as the separation between the midpoints of adjacent ferrite bands separated by cementite lamellae (as defined schematically in Figure 1(c)) and is determined from 10 to 15 SEM micrographs of randomly chosen pearlite colonies. The average is found to be  $190 \pm 24$  nm for a total of 118 measurements. It is to be noted that the IL spacing of the FILSM is significantly lower ( $\sim 44$  pct) than that of the CILSM ( $\sim 275$  nm) (Figure 1(d)).

The microstructural development during cold-rolling is summarized in Figure 2. The 30 pct cold-rolled material shows differently oriented pearlite colonies (Figure 2(a)). The inset in Figure 2(a) shows incipient bending and local fragmentation of the straight-edge lamellae of the starting material (white arrows). The 50 pct cold-rolled material shows lamellae inclined to the RD, indicating the beginning of alignment of the lamellae along the RD (Figure 2(b)). Extensive bending, twisting, and wriggling of the lamellae are noticed (shown inset in Figure 2(b) and marked by arrows). 80 pct cold-rolled material (Figure 2(c)) reveals alignment of the differently oriented lamellae along the RD (Figure 2(c)). Localized bending, fragmentation of the cementite lamellae (marked by arrows), and the presence of shear bands recognized by wavy appearance (arrow in the inset in Figure 2(c)) are noticed. Cold-rolling to 95 pct reduction ((Figure 2(d))) imparts considerable

heterogeneity in the microstructure, as revealed by extremely fine-scale lamellar structure (region enclosed within the ellipse), fragmented regions (marked by arrows) and propagating shear bands. The inset in Figure 2(d) reveals the deformation-induced bulk nanolamellar structure with the presence of shear bands (yellow arrow). The microstructure of the severely cold-rolled FILSM may be compared with the microstructure of the 95 pct cold-rolled CILSM (Figure 2(e)), which shows profuse heterogeneities revealed by extremely fine lamellar regions (enclosed within the ellipse) and considerably fragmented regions (marked by arrows). Further, the area fraction of the fragmented regions is considerably greater in CILSM ( $\sim 0.52$ ) than in the FILSM ( $\sim 0.15$ ).

The variation of the inter-lamellar spacing with an increasing cold-rolling reduction in the FILSM is compared with the CILSM in Figure 3(a). For this purpose, more than a hundred inter-lamellar spacings in each condition were measured manually from several SEM micrographs. The data for the CILSM have been reported by Narayanswamy *et al.*<sup>[26]</sup>. To further compare the experimental trend, the variation of  $\lambda$  with increasing deformation is plotted according to the empirical relationship,<sup>[5]</sup>

$$\lambda = \lambda_0 \exp(-\epsilon) \quad [1]$$

$\lambda_0$  = initial IL spacing,  $\sim 190$  nm and  $275$  nm for FILSM and CILSM, respectively.

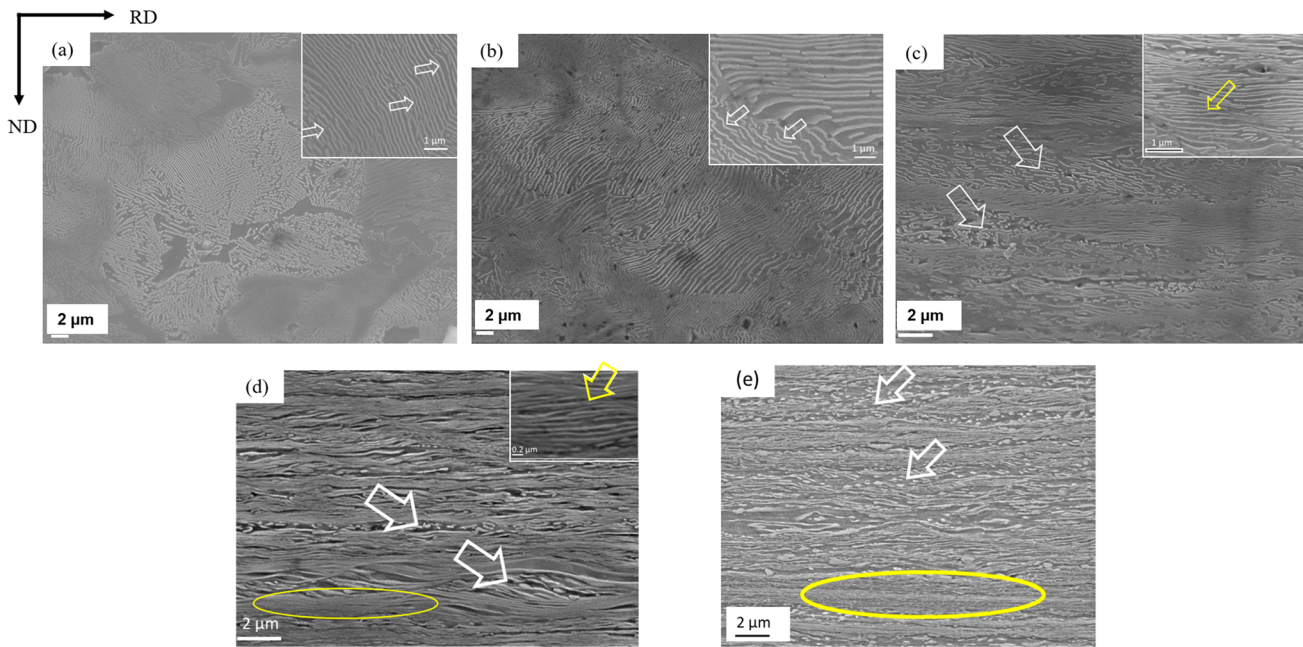


Fig. 2—SEM micrographs of (a) 30 pct, (b) 50 pct, (c) 80 pct, and (d) 95 pct cold-rolled FILSM. (e) The micrograph of the 95 pct cold-rolled CILSM.

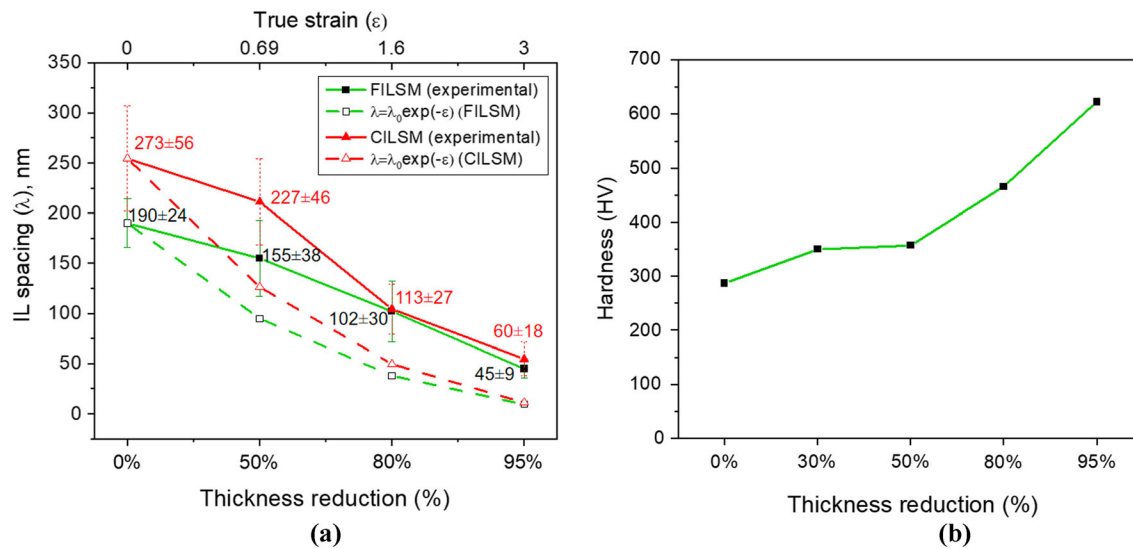


Fig. 3—(a) Variation of ILspacing( $\lambda$ ) with progressing thickness reduction in FILSM is compared with CILSM. (b) The hardness variation in FILSM with increasing thickness reduction.

$\varepsilon$  = true strain.

A consistent decrease in the inter-lamellar spacing with increasing deformation is observed in both materials experimentally. However, the rate of decrease is perceptibly lower than that predicted by the empirical relationship. Further, the rate of decrease in the IL spacing is initially slow in the CILSM up to 50 pct reduction in thickness but increases remarkably beyond that. The FILSM shows a smaller average IL spacing of  $\sim 45 \pm 9$  nm than that of the CILSM specimen of  $\sim 60 \pm 18$  nm after 95 pct deformation. The hardness evolution in the FILSM with increasing strain is

depicted in Figure 3(b). The hardness increases consistently with a decrease in  $\lambda$  with increasing thickness reduction. Noticeably high hardness of  $\sim 623$  HV is obtained after 95 pct cold-rolling.

The texture evolution is summarized by depicting the  $\varphi_2 = 45$  deg sections of the ODFs in Figure 4. The typical textures fibers, namely RD ( $\parallel <110>$ ) and ND ( $\parallel <111>$ ) fibers<sup>[32–34]</sup> are shown overlaid in the ODF sections. The starting FILSM (Figure 4(a)) does not reveal the presence of typical fiber texture due to the presence of differently oriented pearlite colonies. 30 pct (Figure 4(b)) and 50 pct cold-rolled (Figure 4(c))

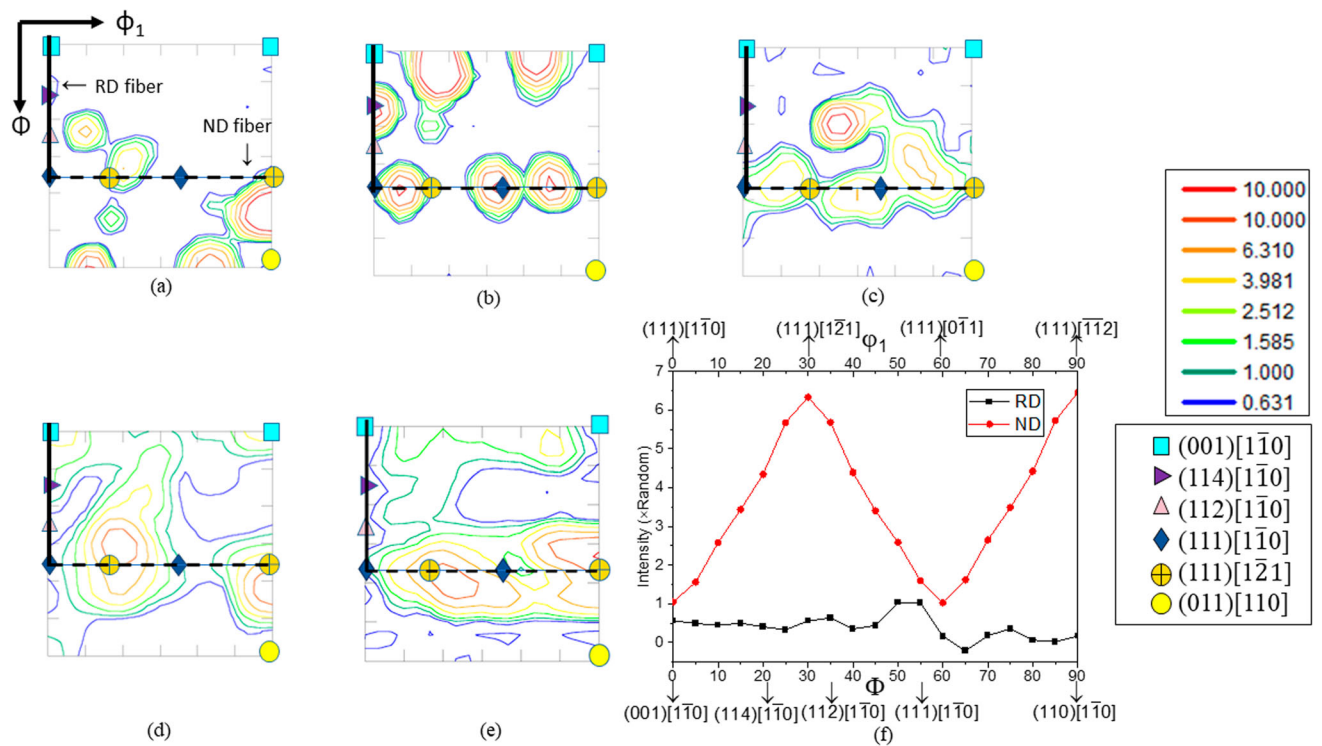


Fig. 4— $\phi_2 = 45$  deg ODF section of the (a) starting FILSM, (b) 30 pct, (c) 50 pct, (d) 80 pct, and (e) 95 pct cold-rolled materials. (f) The intensity distribution along the RD and ND fibers in the 95 pct cold-rolled material.

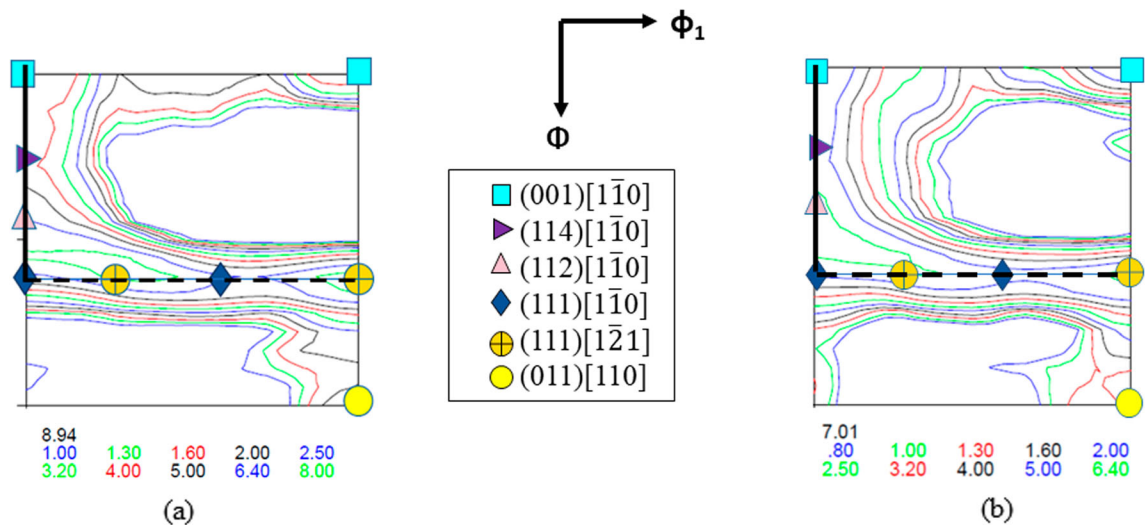


Fig. 5— $\phi_2 = 45$  deg ODF section (macrotecture by XRD) of (a) FILSM and (b) CILSM (reprinted with permission from reference<sup>[26]</sup>) in the 95 pct cold-rolled condition.

materials show orientations along the ND fiber. However, following 80 pct (Figure 4(d)) and 95 pct (Figure 4(e)) reduction, microtexture featured by stronger ND ( $\parallel \langle 111 \rangle$ ) than the RD ( $\parallel \langle 110 \rangle$ ) fiber can be observed. This is amply corroborated by the intensity distribution along the RD and ND fibers in the 95 pct cold-rolled material (Figure 4(f)).

The  $\phi_2 = 45$  deg sections of the ODFs of bulk texture (determined by XRD) of the 95 pct cold-rolled

FILSM (Figure 5(a)) and CILSM (Figure 5(b)) are presented to compare the influence of starting IL on texture development. The ODF sections appear similar, indicating the presence of the characteristic typical RD and ND fiber.

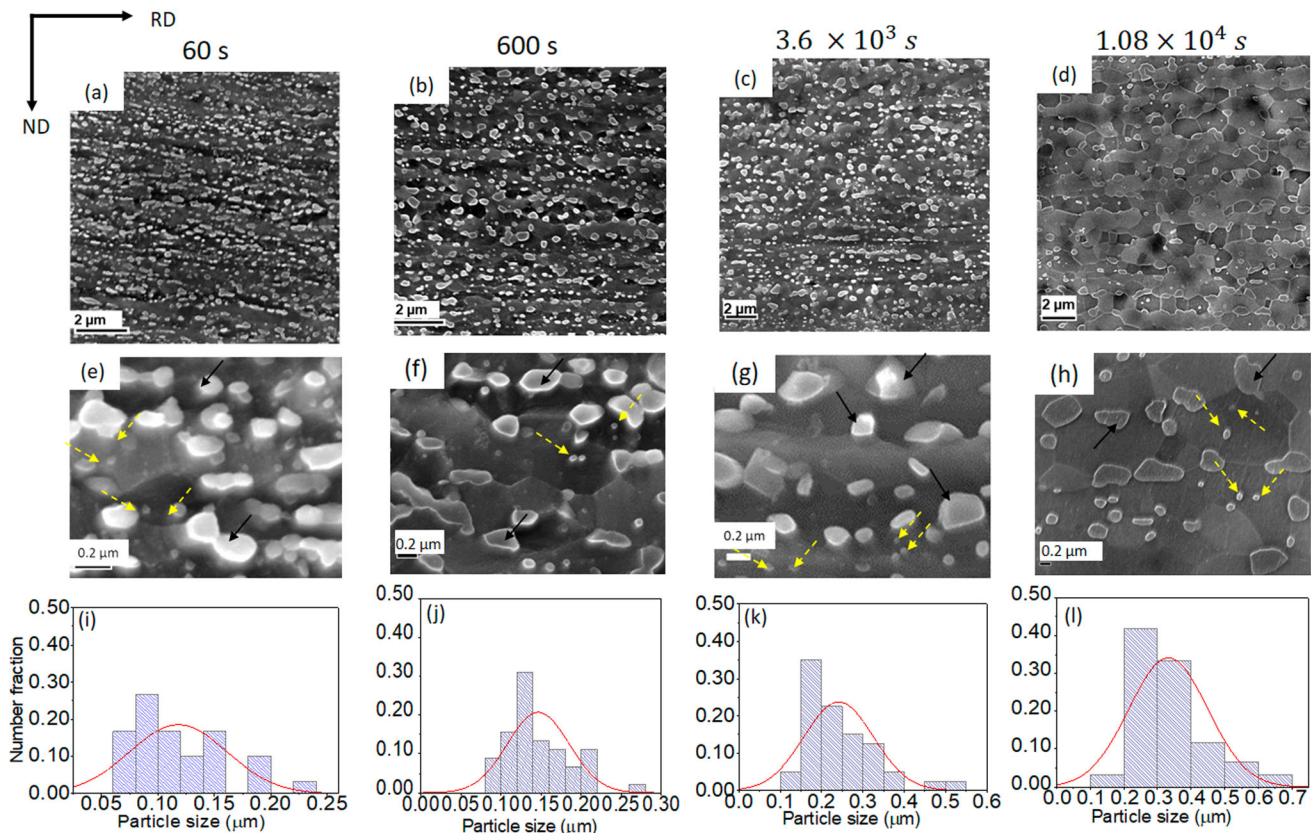


Fig. 6—(a-d) SEM micrographs, (e-h) magnified SEM micrographs reveal dispersion of finer cementite particles located within the grains (shown by yellow arrows) and considerably larger cementite particles are located at the ferrite grain boundaries and the triple points (marked by black arrows), and (i-l) cementite particle size distribution in severely cold-rolled FILSM annealed for (a), (e), (i) 60 s, (b), (f), (j) 600 s, (c), (g), (k)  $3.6 \times 10^3$  s, and (d), (h), (l)  $1.08 \times 10^4$  s (Color figure online).

### B. Effect of Annealing

The effect of isothermal annealing at 973 K (700 °C) on microstructure development of 95 pct cold-rolled material is shown in Figure 6. The large area micrographs of the material annealed for 60 s (1 min) Figure 6(a) confirms complete transformation to a microduplex structure consisting of nanocrystalline ferrite matrix (with average grain size  $\sim 100$  nm) dispersed with spheroidized cementite. The magnified image in Figure 6(e) shows dispersed cementite particles. The micrograph suggests that finer cementite particles are located within the grains (indicated by yellow arrows). In contrast, relatively larger cementite particles are located at the ferrite grain boundaries and the triple points (black arrows). The specimens were annealed for 600 s (10 min) (Figure 6(b)),  $3.6 \times 10^3$  s (60 min) (Figure 6(c)), and  $1.08 \times 10^4$  s (180 min) (Figure 6(d)) and retain the microduplex structure. The size distribution of the cementite particles (Figure 6(i-l)) shows that the particle size remains well within the ultrafine range.

The IPF map of the specimen annealed for 60 s (1 min) (Figure 7(a)) reveals the elongated microstructure extended along the RD. High-angle boundaries (HABs; misorientation angle ( $\theta$ )  $> 15^\circ$ ; black) separate the lamellar ferrite bands along the ND, while profuse low-angle boundaries (LABs;  $\theta \leq 15^\circ$ ; white) network

can be easily observed at the interior of the lamellar bands. The cementite particles appear black (due to being unindexed). The typical misorientation environment inside the ferrite bands is represented by the point-to-point (neighboring) and point-to-origin (cumulative) misorientation plots (shown in Figure 8(a)) along the vector in Figure 7(a). The neighboring profile shows low misorientation typical of sub-grain structure, while the cumulative profile shows high accumulated misorientation. The microstructures of the specimens were annealed for 600 s (10 min) (Figure 7(b)),  $3.6 \times 10^3$  s (60 min) (Figure 7(c)), and  $1.08 \times 10^4$  s (180 min) (Figure 7(d)) and showed a strong resemblance, featured by lamellar ferrite bands containing profuse LAB network and dispersed cementite particles. The internal misorientation of the ferrite bands (along the vectors in Figure 7(c) and Figure 7(d)) in the specimens annealed for  $3.6 \times 10^3$  s (60 min) and  $1.08 \times 10^4$  s (180 min) are also shown (Figure 8(b) and Figure 8(c), respectively). The neighboring misorientation profile shows characteristic spikes indicating the presence of subgrains separated by LABs. The IPF map of the 95 pct cold-rolled CILSM annealed at 923 K (700 °C) for  $3.6 \times 10^3$  s (60 min) is shown for comparison in Figure 7(e). The microstructure of the annealed CILSM resembles that of the annealed FILSM, featured by lamellar ferrite bands containing profuse LAB network

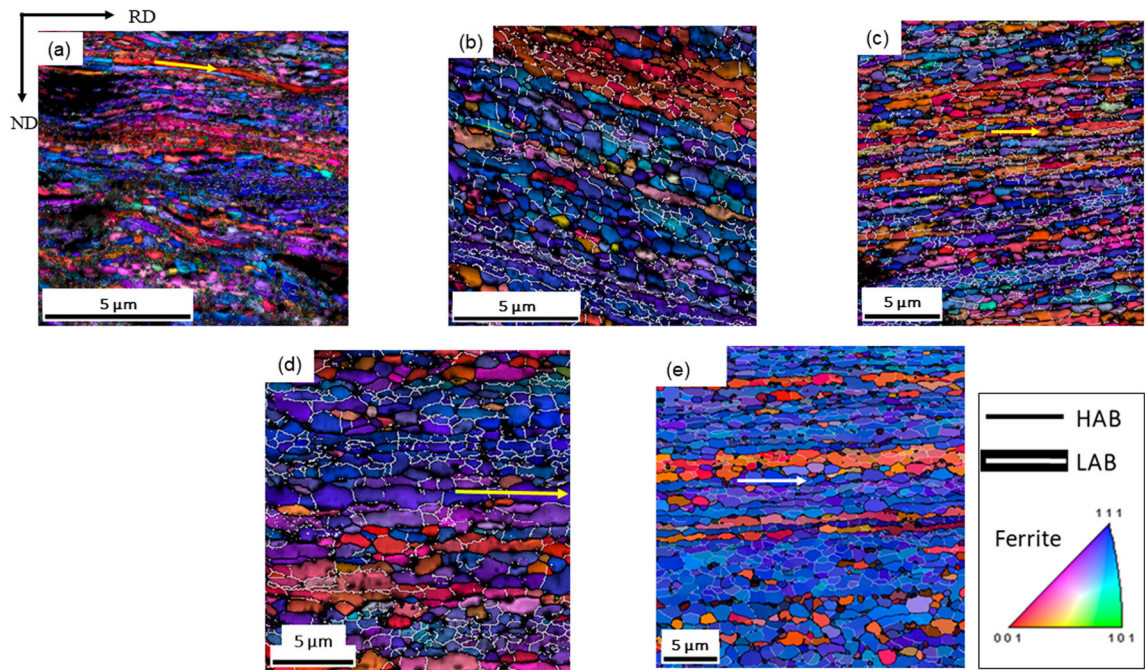


Fig. 7—ND-IPF maps for cold-rolled 95 pct and annealed at 700 °C (973 K) for (a) 60 s, (b) 600 s, (c)  $3.6 \times 10^3$  s, and (d)  $1.08 \times 10^4$  s. The ND-IPF map of the 95 pct cold-rolled + annealed ( $700^\circ/3.6 \times 10^3$  s) CILSM is shown in (e) for comparison. The misorientation profiles along the vectors in (a), (c), (d), and (e) are shown in Fig. 8.

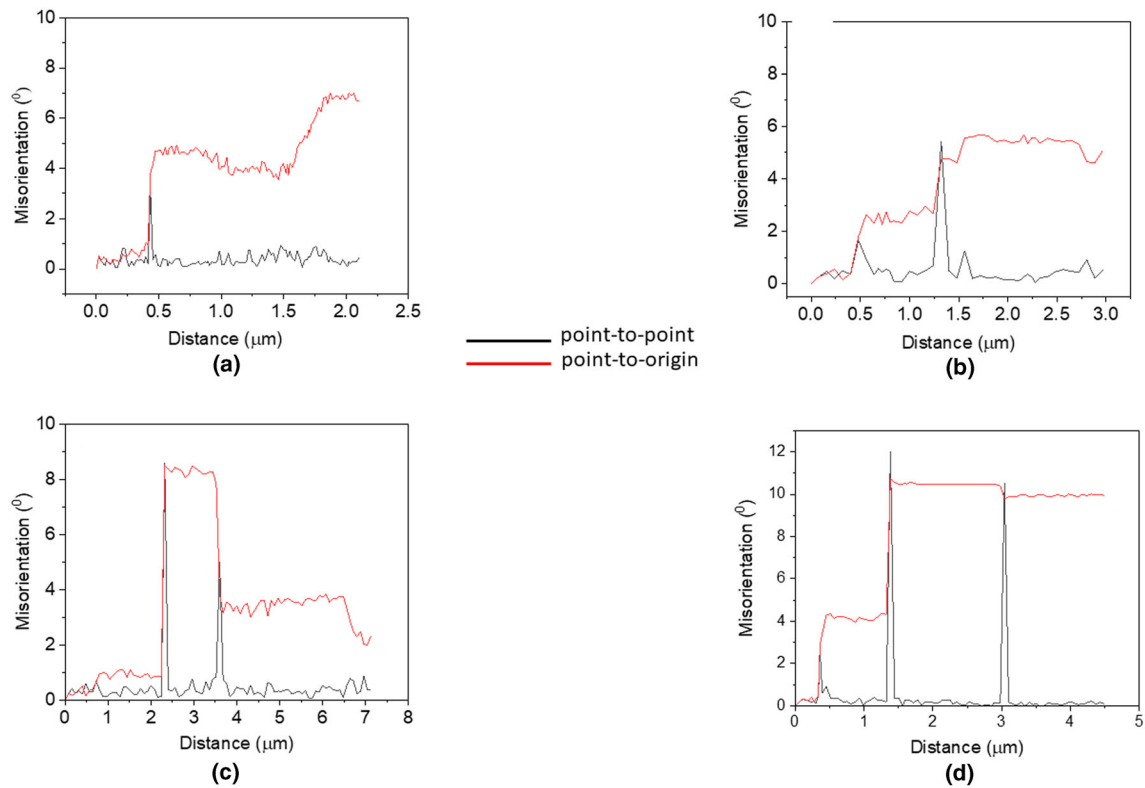


Fig. 8—Misorientation profiles inside the ferrite bands of the FILSM specimens annealed for (a) 60 s, (b)  $3.6 \times 10^3$  s, and (c)  $1.08 \times 10^4$  s. (d) The misorientation profile of the CILSM specimen cold-rolled and annealed for  $3.6 \times 10^3$  s.

and dispersed cementite. The misorientation profiles along the vector in Figure 7(e) are shown in Figure 8(d),

which appear similar to those in different annealed FILSM specimens.

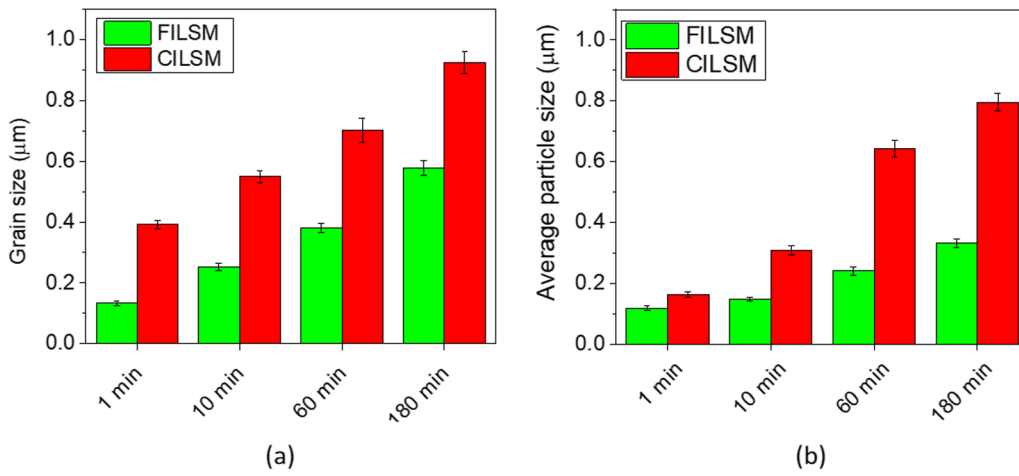


Fig. 9—Dependence of (a) ferrite and (b) cementite size on annealing time in FILSM and CILSM.

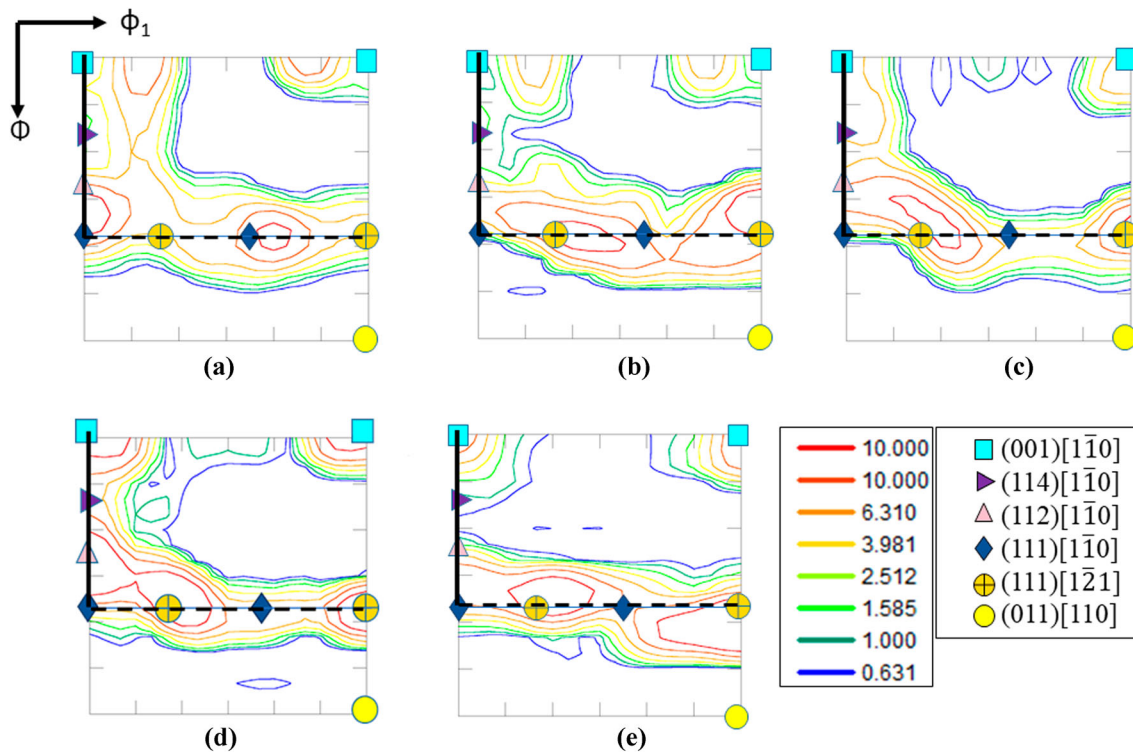


Fig. 10— $\phi_2 = 45$  deg section of the 95 pct cold-rolled FILSM annealed at 700 °C for (a) 60 s, (b) 600 s, (c)  $3.6 \times 10^3$  s, and (d)  $1.08 \times 10^4$  s. The ODF section of the 95 pct cold-rolled + annealed (700 °C/ $3.6 \times 10^3$  s) CILSM is compared in (e) (reprinted with permission from reference<sup>[26]</sup>).

The variation in the mean size of ferrite (Figure 9(a)) and cementite (Figure 9(b)) with annealing temperature in FILSM and CILSM are compared. The data pertaining to CILSM are obtained by analyzing the microstructures reported by Narayanswamy *et al.*<sup>[26]</sup>. The grain size is calculated from the EBSD maps considering only the spacing between the HABs. The FILSM remarkably shows a nanocrystalline ferrite grain size of ~250 nm after annealing for 60 s (1 min), which increases with increasing annealing time to ~850 nm after an annealing interval of  $1.08 \times 10^4$  s (180 min). Nevertheless, the annealed FILSM specimens

consistently show smaller ferrite grain sizes than those of the CILSM specimens (Figure 9(a)).

The variation of the cementite particle size shows a similar trend (Figure 9(b)), increasing with increasing annealing time. The average size of the cementite particles in the FILSM is ~118 nm in the 60 s (1 min) annealed specimen, which increases to ~300 nm upon annealing for  $1.08 \times 10^4$  s (180 min). The average cementite particle size in the FILSM specimens after different annealing treatments is found to be consistently lower compared to those of their CILSM counterparts.



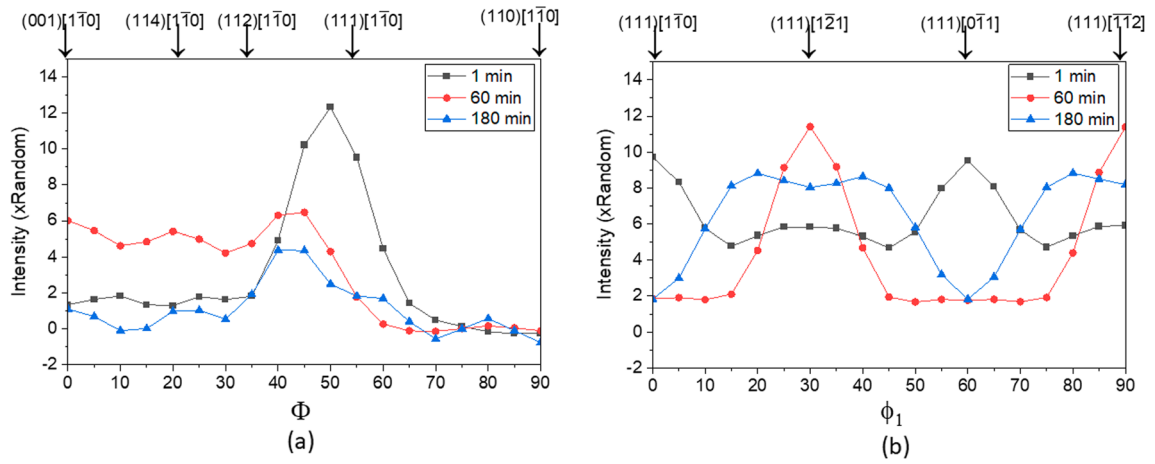


Fig. 11—Intensity variation along the (a) RD and (b) ND fiber of ferrite in annealed FILSM.

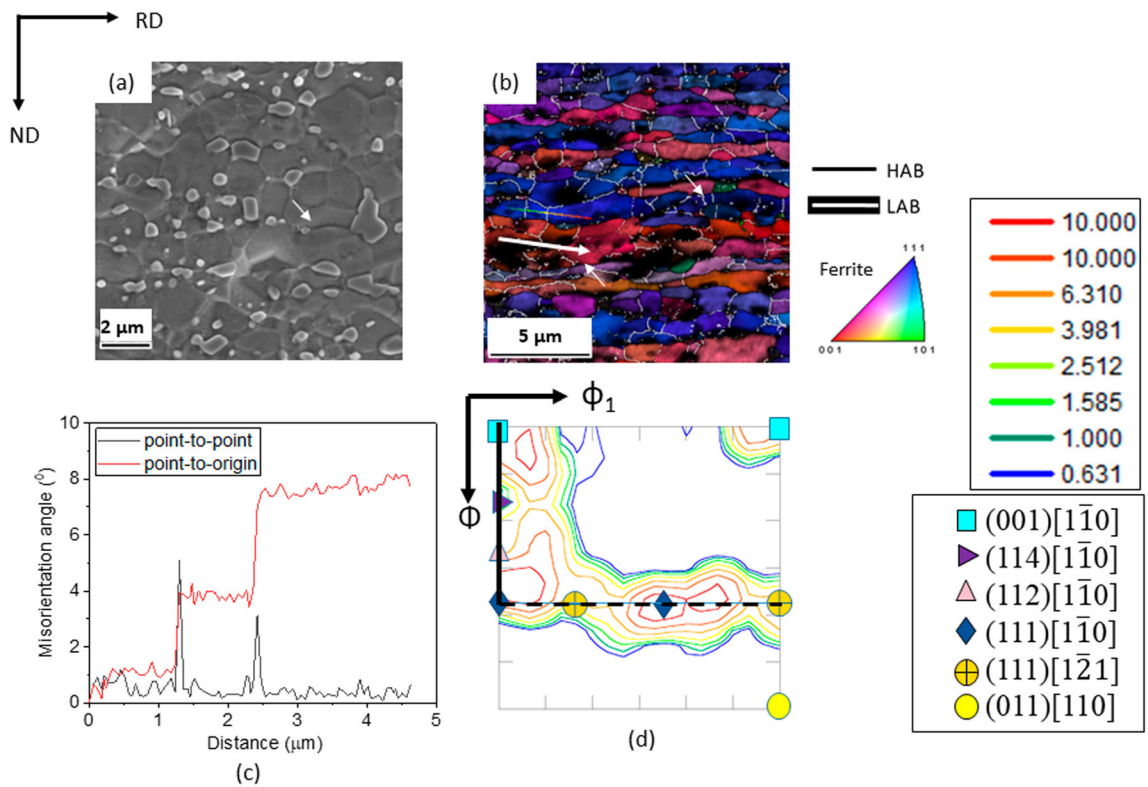


Fig. 12—(a) SEM micrograph and (b) ND-IPF map of the 95 pct cold-rolled FILSM annealed for  $4.32 \times 10^4$  s (720 min). (c) The neighboring and cumulative misorientation profile along the vector in (b). (d) The  $\phi_2 = 45$  deg section of the ODF.

The  $\phi_2 = 45$  deg sections summarize the textures of the annealed FILSM specimens in Figure 10. The 60 s (1 min) (Figure 10(a)) annealed specimen confirms orientations along the typical RD and ND fiber. However, the ND fiber emerges stronger than the RD fiber. Local orientation peaks appear with  $\langle 001 \rangle // \text{ND}$  alongside the two typical texture fiber components. The ODF sections of the specimens annealed for 600 s (10 min) (Figure 10(b)) continue to show similar features. Annealing for 60 min (Figure 10(c)) weakens the

discrete orientations with  $\langle 001 \rangle // \text{ND}$ . The  $\{001\} \langle 100 \rangle$  orientation on the RD fiber is strengthened, whereas the ND fiber (ND//  $\langle 111 \rangle$ ) appears quite prominent. Annealing for  $1.08 \times 10^4$  s (180 min) (Figure 10(d)) leads to further strengthening of the  $\{001\} \langle 100 \rangle$  component. The ND fiber (ND//  $\langle 111 \rangle$ ) shows only minor changes. The 95 pct cold-rolled + annealed ( $700^\circ\text{C}/3.6 \times 10^3$  s (60 min)) CILSM shows very similar texture development.

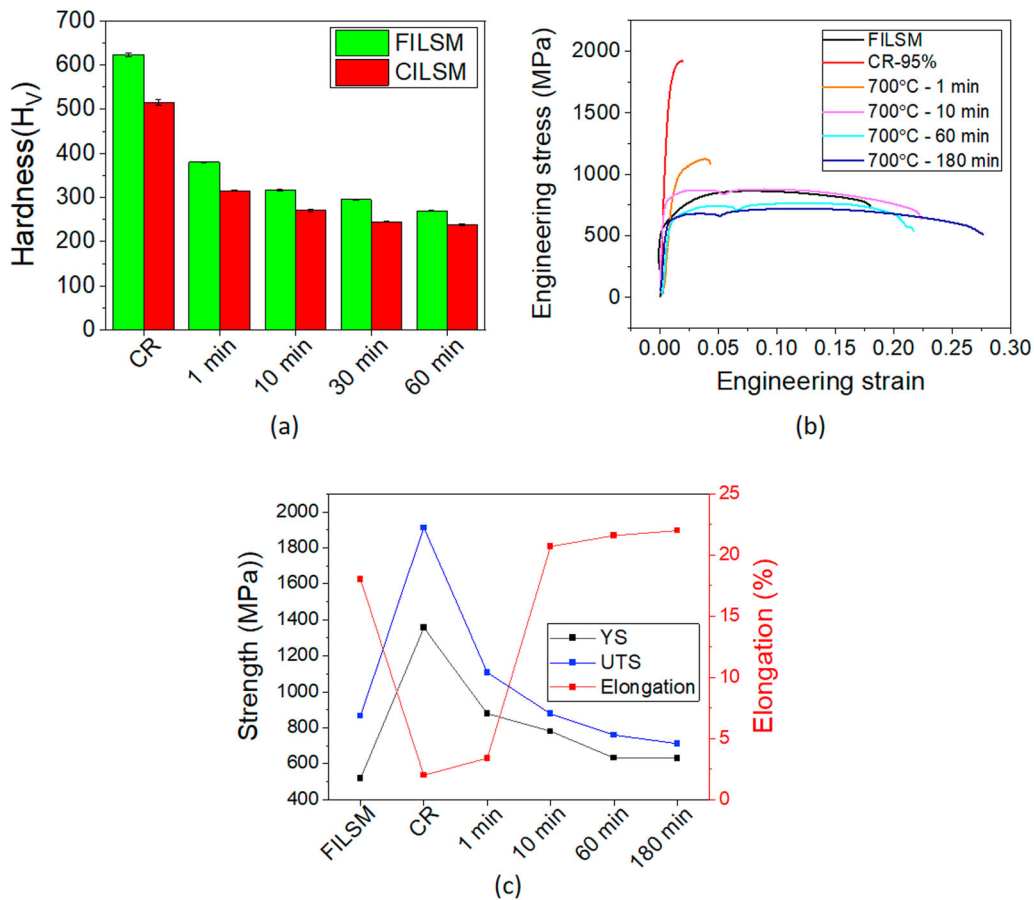


Fig. 13—(a) Hardness variation with increasing annealing time in 95 pct cold-rolled FILSM is compared with CILSM. (b) The tensile curves for the FILSM. (c) Strength–ductility variation vs. annealing time in FILSM.

The texture evolution is compared by plotting the intensities along the typical fibers in Figure 11. As may be understood from Figure 11(a), the intensity of the RD fiber gradually decreases with increasing annealing time. The peak intensity is located in the vicinity of  $\varphi = 45 \text{ deg}-55^\circ$ , which corresponds to the scatter around the  $\{111\} \langle 110 \rangle$  orientation lying at the intersection of the RD and ND fibers. In contrast, Figure 11(b) depicts that the peak intensity along the ND fiber shifts remarkably depending upon the annealing time. The intensity peak is located in the vicinity of the  $\{111\} \langle 110 \rangle$  orientation for the specimen annealed for 1 min, whereas for the specimens annealed for longer annealing intervals of  $3.6 \times 10^3 \text{ s}$  (60 min) and  $1.08 \times 10^4 \text{ s}$  (180 min), the peak intensity is shifted to the  $\{111\} \langle 112 \rangle$  orientation.

The effect of prolonged annealing for  $4.32 \times 10^4 \text{ s}$  (720 min) is shown in Figure 12. The retention of the elongated ferrite bands containing coarse cementite particles is observed in Figure 12(a). The elongated bands are separated along the ND by HABs extended parallel to the RD (Figure 12(b)). In contrast, the bands are internally divided by LABs which frequently run perpendicular or slightly inclined to the bands (white arrows in Figures. 12(a) and (b)). The neighboring misorientation shows low values, while the cumulative misorientation

confirms large accumulated values (Figure 12(c)). The  $\varphi_2 = 45 \text{ deg}$  section shows discrete orientation maximum at the  $\{001\} \langle 100 \rangle$  location on the RD fiber. In contrast, a dominant  $\{111\} \langle 110 \rangle$  component is also observed at the intersection of the RD and ND fiber (Figure 12(d)).

The effect of annealing on mechanical response is understood from the hardness variation (Figure 13(a)). A reduction in hardness with increasing annealing time is observed for both FILSM and CILSM, although the FILSM specimens show consistently higher hardness than the corresponding CILSM specimens. To further understand the mechanical behavior, tensile tests are carried out. The variation of YS, UTS, and elongation of the FILSM is shown in Figure 13(b). The YS and UTS of the FILSM are increased after severe cold-rolling at the expense of elongation. The strength decreases while the elongation increases with increasing annealing time. An appreciable strength–ductility combination is achieved after annealing for 600 s (10 min).

## IV. DISCUSSION

### A. Effect of Cold-Rolling

The microstructural evolution in the cold-rolled FILSM is characterized by local fragmentation and bending of the lamellae at low deformation (after 30 pct reduction), progressive alignment of the lamellae along the RD (beyond 50 pct reduction), formation of wavy shear bands (after 80 pct reduction), and finally, formation of an extremely fine lamellar structure with considerable local heterogeneities in the form of wavy sheared and considerably fragmented regions (after 95 pct reduction). Interestingly, Furuhashi *et al.*<sup>[25]</sup> have also highlighted a similar complex microstructural evolution pathway. The microstructural evolution pattern is consistent with the observations presented here. Although Furuhashi *et al.*<sup>[25]</sup> have not reported extensive cementite fragmentation, considerable fragmentation observed here is consistent with high-pressure torsion (HPT) results.<sup>[35–37]</sup>

Despite the microstructural evolution pattern of FILSM closely resembling that of the CILSM, it is worth noting that the microstructure of the CILSM appears to show more inhomogeneities, including abundant fragmented regions even after 95 pct cold-rolling. The greater fragmentation and heterogeneities in the CILSM appear consistent with the ease of severe bending, nucleation, and propagation of kink and shear bands owing to the larger inter-lamellar spacing. Remarkably, the difference in the inter-lamellar spacing also considerably affects further microstructural refinement during cold-rolling. A finer inter-lamellar spacing in FILSM results in a smaller inter-lamellar spacing than CILSM after severe deformation to 95 pct cold-rolling. The present observations resemble the effect of starting grain size; a finer starting grain size leads to a finer grain size following severe deformation. Nevertheless, experimentally measured values of the inter-lamellar spacing are considerably lower than the predicted values for both FILSM and CILSM. These lower observed values may also be contributed, among other factors, by the severe bending and fragmentation accommodating the imparted strain. As a result, the imposed strain during cold-rolling does not contribute totally to the refinement of the inter-lamellar spacing. These outcomes lead to the observed differences in the experimental and predicted values of the inter-lamellar spacing.

The texture development follows a familiar trend in the FILSM and CILSM. The weak diffuse texture at lower deformation levels is strengthened with increasing cold-rolling strain. The development of the typical deformation texture featured by the typical RD and ND fibers is observed beyond 80 pct cold-rolling. The texture is further strengthened after 95 pct cold-rolling. However, a certain difference in micro- and macrotexture could be observed. The macrotexture shows the presence of prominent RD and ND fibers, whereas the microtexture shows somewhat stronger ND fiber components. These differences in macro- and microtextures

are associated with the observed microstructural heterogeneities, which can significantly affect the local texture formation.

### B. Microstructure and Texture After Annealing

The microstructure of the 60 s (1 min) annealed specimen shows complete spheroidization of the cementite. However, the elongated lamellar banded structure is retained with a profuse LAB network inside the bands. The elongated bands separated by HABs show neighboring misorientation spikes alongside large cumulative misorientation. These features indicate the existence of substructures inside these bands, consistent with microstructural evolution by extended recovery or continuous recrystallization.

A strain-dependent gradual transition from discontinuous to continuous recrystallization has been reported previously in CILSM.<sup>[26]</sup> The continued fragmentation of cementite with progressive deformation results in the redistribution of extremely fine cementite in the primary ferrite regions, which effectively pin the movement of the HABs and hinder discontinuous recrystallization. On the other hand, as observed in severely cold-rolled FILSM and CILSM, long-range HAB migration along the ND in fine pearlitic regions is greatly hindered by the pinning effect originating from the rapid spheroidization of nanoscale cementite at the same time, as already observed. Consequently, discontinuous recrystallization by large distance migration of HABs is effectively hindered in favor of a process of extended recovery or continuous recrystallization. The recovery-dominated process observed in the FILSM and CILSM occurs as a continuous process throughout the microstructure.<sup>[5]</sup>

Despite the apparent similarities in the annealing behavior and microstructure evolution in the severely cold-rolled FILSM and CILSM, a significant impact of the starting IL spacing can yet be recognized. The FILSM shows finer ferrite grain sizes in the different annealed conditions. The finer ferrite size in the annealed FILSM is consistent with the smaller IL spacing in the 95 pct cold-rolled FILSM. Since large HAB migration is hindered during annealing in both FILSM and CILSM, smaller IL spacing in the 95 pct cold-rolled FILSM results in a decidedly finer ferrite grain size after different annealing treatments. The microstructure is quite stable against grain growth, as may be evidenced by the near ultrafine ferrite grain size of  $\sim 1.7 \mu\text{m}$  for an annealing interval of  $4.32 \times 10^4$  s (720 min/12 h).

The finer cementite particle size in the annealed FILSM than that of the CILSM is also noteworthy. It is perceived that process of spheroidization involves activities of deformation inhomogeneities (kinks) formed during severe deformation.<sup>[28,30]</sup> The local curvature differences associated with kinks result in an increased equilibrium carbon concentration in the vicinity of the kinks than in the regions away from the kinks in the vicinity of the flat surfaces of the lamellae. Thus, the

**Table II. Experimentally Calculated Parameters for Determining the H-P Plot in Figure 14**

Annealing time (s)	$d_{gr}$ (nm)	L (nm)	d (nm)	$\sigma_{O-A}$ (MPa)	$\sigma_{YS}$ (MPa)	$\sigma_{YS} - \sigma_{O-A}$ (MPa)
60	46	201	323	89.2	883.3	794
600	60	260	514	73.2	741	667.8
$3.6 \times 10^3$	103	502	546	40.8	655	614.2
$1.08 \times 10^4$	167	870	856	25.3	603	577.7

onset of the process of spheroidization is driven by inhomogeneous carbon diffusion owing to the chemical potential difference along the kink surfaces (Gibbs–Thomson effect). In turn, this phenomenon leads to the fast dissolution of the kinks, enabling fragmentation and subsequent/concurrent spheroidization of the cementite.<sup>[28]</sup> Interestingly, the cementite particles show an evident dependence on the starting IL spacing, a smaller average size in the FILSM. Although direct evidence could not be presented here, it is perceived that the formation of more abundant kinks with local curvature differences in the FILSM leads to smaller fragmentation lengths and smaller cementite particle sizes after different annealing treatments.

Subsequent to the spheroidization process, redistribution of cementite may take place. Due to the higher carbon concentration in the vicinity of the finer cementite particles, the solute carbon diffusion may occur toward the interior of the ferrite grains with lower carbon concentration and subsequent reprecipitation. For prolonged annealing, faster diffusion through grain boundaries favors the growth of the grain boundary and triple-point cementite particles by the Ostwald-ripening process.

The development of annealing texture in the severely deformed FILSM may be discussed in the context of the microstructure development mechanism. The annealing texture with dominant RD and ND fiber components appears very similar to the deformation texture. The pattern of annealing texture evolution is thus similar to that in the CILSM, which also shows no significant changes in texture upon annealing. Since the microstructural evolution due to recovery or continuous recrystallization happens without long-range HAB migration (as discussed previously), no major change in texture is expected in both FILSM and CILSM. The extended recovery (or continuous recrystallization)-dominated behavior is supported by the texture of the 95 pct cold-rolled FILSM subjected to prolonged annealing treatment for  $4.32 \times 10^4$  s (720 min). The texture of the specimen shows no major differences from the texture observed in other annealed conditions, thus confirming the retention of deformation texture after different annealing treatments consistent with recovery behavior.<sup>[5]</sup> Nevertheless, minor changes or shifts in the local intensity can be recognized in the ODFs of the specimens annealed for different annealing intervals. These minor differences in texture appear to originate from the subgrain growth by sub-boundary migration or sub-grain rotation and coalescence associated with the recovery process.

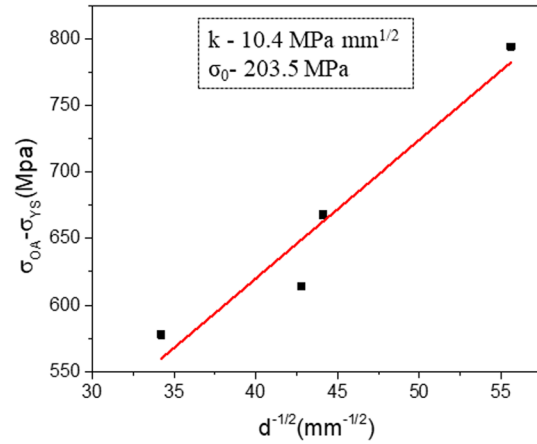


Fig. 14—H-P plot for the annealed steels.

The largest change in both hardness and strength happens immediately after annealing for 60 s. The significant decrease in hardness is concomitant with dislocation annihilation and rearrangement typical for recovery processes and spheroidization of cementite. The hardness decreases further with increasing annealing time due to a simultaneous increase in the ferrite grain size and cementite particle size. The higher hardness in the annealed FILSM specimens compared to the corresponding CILSM specimens is consistent with the finer average ferrite and cementite size in the former. The higher hardness of the FILSM agrees quite well with the greater YS and UTS of the FILSM. The nanosized cementite particles with incoherent interfaces with the ferrite matrix considerably improve the strength of the annealed UFG FILSM.

The yield strength of the annealed materials ( $\sigma_{YS}$ ) can be considered as the linear addition of (a) Hall–Petch ( $\sigma_{H-P}$ ) and (b) Orowan–Asby ( $\sigma_{O-A}$ ) strengthening, as may be expressed by the following equation:

$$\sigma_{YS} = \sigma_{H-P} + \sigma_{O-A} \quad [2]$$

Therefore,

$$\sigma_{YS} - \sigma_{O-A} = \sigma_{H-P} = \sigma_0 + \frac{k}{\sqrt{d}} \quad [3]$$

where  $\sigma_0$  is the lattice fraction stress,  $k$  is the H-P coefficient, and  $d$  is the mean ferrite grain size.

The large cementite particles located at the grain boundaries and triple points do not contribute to O-A strengthening. Therefore, the following modified Orowan-Asby equation<sup>[38]</sup> can be used:

$$\sigma_{O-A} = M \frac{0.84Gb}{2\pi(1-\nu)^{1/2}(L-d_{gi})} \ln\left(\frac{d_{gi}}{2b}\right) \quad [4]$$

where

Taylor factor (M) = 2.8 for BCC, shear modulus (G) = 77,000 MPa, burgers vector (b) = 0.248 nm, Poisson ratio ( $\nu$ ) = 0.3,  $d_{gi}$  is the mean cementite particle diameter located within the grain interiors, and L is the mean inter-particle spacing.

The experimentally determined values of the above parameters for different annealed materials are tabulated in Table II and used to construct the plot of  $\sigma_{YS} - \sigma_{O-A}$  vs.  $d^{-1/2}$  according to the equation (iii) in Figure 14, which shows a good linear fit. The H-P coefficient  $k$  is  $\sim 11$  MPa  $\text{mm}^{1/2}$  ( $329$  MPa  $\mu\text{m}^{1/2}$ ). The H-P coefficient has been reported to be increased by carbon concentration, particularly at the grain boundaries. The experimental value of the H-P coefficient lies within the range reported for steels having carbon segregation at the grain boundaries ( $315\text{--}760$  MPa  $\mu\text{m}^{0.5}$ ).<sup>[39,40]</sup> Interestingly, carbon segregation at the ferrite boundaries has been confirmed in severe wire-drawn and annealed steels by atom probe analysis.<sup>[10]</sup> However, this aspect has not been confirmed in the present study and should be an aspect of interest in future research.

## V. CONCLUSIONS

The effect of starting IL spacing on the microstructure, texture, and mechanical properties of pearlite was investigated in the present research. For this purpose, pearlite steel was heat-treated to achieve FILSM specimens with an IL spacing of 190 nm and compared with previously studied CILSM with an IL spacing of  $\sim 275$  nm. The two starting materials were cold-rolled to 95 pct reduction and heat-treated at 923 K (700 °C) for different time intervals. The following conclusions can be summarized:

- (i) Irrespective of the starting IL spacing, the microstructure evolution during cold-rolling showed progressive alignment of the pearlitic colonies along the RD, bending and kink morphologies, fragmentation of cementite, and the evolution of deformation-induced nanoscale structure finally. However, a finer starting IL spacing in the FILSM resulted in a lower IL spacing ( $\sim 45$  nm) than in the CILSM ( $\sim 60$  nm).
- (ii) Progressive texture strengthening during cold-rolling resulted in the typical RD and ND fiber-dominated texture. The bulk texture analysis indicated the development of similar deformation textures for FILSM and CILSM.

- (iii) The annealing-induced rapid spheroidization of cementite resulted in a microduplex structure with ferrite matrix and nanosized spheroidized cementite in both FILSM and CILSM. The strong pinning effect exerted by cementite particles promoted recovery or continuous recrystallization. Despite the similarities in the annealing behavior, starting IL spacing affects the microstructure development, manifested by consistently lower ferrite and cementite size in FILSM than those in the CILSM.
- (iv) The texture development after annealing was very similar in FILSM and CILSM, and amply corroborated with the recovery process. Thus, the starting IL spacing affected the microstructure evolution more significantly than texture formation.
- (v) Annealed microduplex structures showed the H-P coefficient falling within the range for steels having carbon segregation at the grain boundaries.

## ACKNOWLEDGMENTS

The authors would like to acknowledge the financial support of the DST-FIST program (under Grant No. SR/FST/ETI-421/2016).

## DATA AVAILABILITY

The data analyzed in this work may be available from the corresponding author upon reasonable request.

## CONFLICT OF INTEREST

The authors have no conflict of interest.

## REFERENCES

1. R.Z. Valiev, R.K. Islamgaliev, and I.V. Alexandrov: *Prog. Mater. Sci.*, 2000, vol. 45, pp. 103–89.
2. A.P. Zhilyaev and T.G. Langdon: *Prog. Mater. Sci.*, 2008, vol. 53, pp. 893–979.
3. R.Z. Valiev and T.G. Langdon: *Prog. Mater. Sci.*, 2006, vol. 51, pp. 881–981.
4. N. Tsuji, Y. Saito, S.H. Lee, and Y. Minamino: *Adv. Eng. Mater.*, 2003, vol. 5(5), pp. 338–44.
5. F.J. Humphreys and M. Hatherly: *Recrystallization and Related Annealing Phenomena*, 2nd ed. Elsevier, Oxford, 2004.
6. B. Verlinden, J. Driver, I. Samajdar, and R.D. Doherty: *Thermo-Mechanical Processing of Metallic Materials*, 1st ed. Elsevier, Amsterdam, 2007.
7. H.K.D.H. Bhadeshia: *Theory of Transformations in Steels*, 1st edn. CRC Press, Boca Raton, 2021.
8. A. Hohenwarter, B. Völker, M.W. Kapp, Y. Li, S. Goto, D. Raabe, and R. Pippan: *Sci. Rep.*, 2016, vol. 6, p. 33228.
9. Y.J. Li, P. Choi, S. Goto, C. Borchers, D. Raabe, and R. Kirchheim: *Ultramicroscopy*, 2013, vol. 132, pp. 233–38.
10. Y.J. Li, P. Choi, S. Goto, C. Borchers, D. Raabe, and R. Kirchheim: *Acta Mater.*, 2012, vol. 60(9), pp. 4005–16.

11. Y.J. Li, P. Choi, C. Borchers, Y.Z. Chen, S. Goto, D. Raabe, and R. Kirchheim: *Ultramicroscopy*, 2011, vol. 111(6), pp. 628–32.
12. X. Zhang, N. Hansen, A. Godfrey, and X. Huang: *Acta Mater.*, 2016, vol. 114, pp. 176–83.
13. X. Zhang, A. Godfrey, N. Hansen, and X. Huang: *Acta Mater.*, 2013, vol. 61, pp. 4898–4909.
14. J. Takahashi, M. Kosaka, K. Kawakami, and T. Tarui: *Acta Mater.*, 2012, vol. 60, pp. 387–95.
15. X. Zhang, A. Godfrey, X. Huang, N. Hansen, and Q. Liu: *Acta Mater.*, 2011, vol. 59, pp. 3422–30.
16. Y. Ivanisenko, W. Lojkowski, R.Z. Valiev, and N.H.J. Fecht: *Acta Mater.*, 2003, vol. 51, pp. 5555–70.
17. M. Zelin: *Acta Mater.*, 2002, vol. 50, pp. 4431–447.
18. S. Das Bakshi, A. Leiro, B. Prakash and H. K. D. H. Bhadeshia: *Mater. Sci. Technol.*, 2015, vol. 31, pp. 1735–44.
19. R. Qin, Y. Luo, B. Elliott-Bowman, and O. Omoigbade: *Mater. Sci. Technol.*, 2018, vol. 34, pp. 29–34.
20. Y. Yasuda, T. Ohashi, T. Shimokawa, and T. Niiyama: *Mater. Sci. Technol.*, 2018, vol. 34, pp. 772–79.
21. K. Mishra, A. Pachauri, and A. Singh: *Tribol. Lett.*, 2018, vol. 66, pp. 1–2.
22. C. Borchers and R. Kirchheim: *Prog. Mater. Sci.*, 2016, vol. 82, pp. 405–44.
23. X. Zhang, A. Godfrey, N. Hansen, X. Huang, W. Liu, and Q. Liu: *Mater. Charact.*, 2010, vol. 61, pp. 65–72.
24. S. Tagashira, K. Sakai, T. Furuhashi, and T. Maki: *ISIJ Int.*, 2000, vol. 40, pp. 1149–56.
25. T. Furuhashi, T. Mizoguchi, and T. Maki: *ISIJ Int.*, 2005, vol. 45, pp. 392–98.
26. S. Narayanswamy, R. Saha, and P.P. Bhattacharjee: *Mater. Charact.*, 2020, vol. 169, 110583.
27. L. Storojeva, R. Kaspar, and D. Ponge: *ISIJ Int.*, 2004, vol. 44, pp. 1211–16.
28. L. Storojeva, D. Ponge, R. Kaspar, and D. Raabe: *Acta Mater.*, 2004, vol. 52(8), pp. 2209–20.
29. N. Jia, Y.F. Shen, J.W. Liang, X.W. Feng, H.B. Wang and R. D. K. Misra: *Sci. Rep.*, 2017, vol. 7, pp. 2679.
30. C. Prasad, P. Bhuyan, C. Kaithwas, R. Saha, and S. Mandal: *Mater. Des.*, 2018, vol. 139, pp. 324–35.
31. S. Narayanswamy, S.R. Reddy, R. Saha, and P.P. Bhattacharjee: *Mater. Sci. Technol.*, 2019, vol. 35, pp. 437–47.
32. F. Emren and U. von Schlippenbach: *Acta Mater.*, 1986, vol. 34, pp. 2105–17.
33. R.K. Ray and J.J. Jonas: *Int. Mater. Rev.*, 1990, vol. 35, pp. 1–36.
34. R.K. Ray, J.J. Jonas, and R.E. Hook: *Int. Mater. Rev.*, 1994, vol. 39, pp. 129–72.
35. J.L. Ning, Y. Ivanisenko, D. Wang, M.Y. Murashkin, and H.J. Fecht: *Mater. Sci. Forum*, 2011, vol. 667, pp. 199–204.
36. F. Wetscher, B.H. Tian, R. Stock, and R. Pippan: *Mater. Sci. Forum*, 2006, vol. 503, pp. 455–60.
37. M.W. Kapp, A. Hohenwarter, S. Wurster, B. Yang, and R. Pippan: *Acta Mater.*, 2016, vol. 106, pp. 239–48.
38. J.L. Ning, Y.L. Feng, and J. Li: *Mater. Sci. Forum*, 2016, vol. 848, pp. 593–606.
39. B. Mintz: *Met. Technol.*, 1984, vol. 11, pp. 265–72.
40. B. Mintz, H. Ke, and G.D.W. Smith: *Mater. Sci. Technol.*, 1992, vol. 8, pp. 537–40.

**Publisher's Note** Springer Nature remains neutral with regard to jurisdictional claims in published maps and institutional affiliations.

Springer Nature or its licensor (e.g. a society or other partner) holds exclusive rights to this article under a publishing agreement with the author(s) or other rightsholder(s); author self-archiving of the accepted manuscript version of this article is solely governed by the terms of such publishing agreement and applicable law.